



Title	Application of non-destructive integrated CT-XRD method to investigate alteration of cementitious materials subjected to high temperature and pure water
Author(s)	Takahashi, Hayato; Sugiyama, Takafumi
Citation	Construction and building materials, 203, 579-588 https://doi.org/10.1016/j.conbuildmat.2019.01.128
Issue Date	2019-04-10
Doc URL	http://hdl.handle.net/2115/80961
Rights	© 2019. This manuscript version is made available under the CC-BY-NC-ND 4.0 license http://creativecommons.org/licenses/by-nc-nd/4.0/
Rights(URL)	http://creativecommons.org/licenses/by-nc-nd/4.0/
Type	article (author version)
File Information	Takahashi_CBM2019.pdf



[Instructions for use](#)

1 **Application of non-destructive integrated CT-XRD method to investigate alteration**
2 **of cementitious materials subjected to high temperature and pure water**
3

4
5 Hayato Takahashi^{1*}, Takafumi Sugiyama²
6

7 ¹ Ph.D. student, Division of Field Engineering for the Environment,
8 Graduate School of Engineering, Hokkaido University, Japan

9 *Corresponding author: Kita-ku Kita-13 Nishi-8, Sapporo, Hokkaido, Japan
10 t1e2k1e7_slugger@eng.hokudai.ac.jp

11 ² Professor, Division of Field Engineering for the Environment,
12 Faculty of Engineering, Hokkaido University, Japan
13
14

15 **Abstract**
16

17 In order to analyze the alteration mechanism after the exposure to various maximum
18 temperatures and immersion in pure water, non-destructive integrated CT-XRD method
19 (the CT-XRD) was applied. Firstly, the verification of the CT-XRD was carried out to
20 compare with conventional powder X-ray diffraction. It revealed that the CT-XRD could
21 evaluate the crystals properly with a given limitation for low energy band. Besides, the
22 CT-XRD indicated the advantage that can detect the presence of crystals which cannot
23 be detected after grinding in preparing the powder sample for the conventional powder
24 XRD. Then, the carbonated cement paste that was heated at 200, 400, 600, and 800 °C
25 followed by immersion in pure water was evaluated by the CT-XRD. The results suggest
26 that sample heated at 400 °C showed the resistance of leaching at most. In addition,
27 rehydration of clinker minerals generated due to heating at 800 °C could be identified
28 although the hydration product was easily dissolved into water.
29

1. Introduction

Although concrete is non-combustible materials for construction, exposure to high temperatures can lead to severe deterioration. While the properties of cement pastes mainly account for the durability of concrete, exposure to high temperature causes the alteration firstly in cement paste, such as moisture transport in pore structures, dehydration of cement pastes, cracking, and so forth. Therefore, it should be needed to clarify the alteration of cement paste by high temperature.

A variety of research was reported to clarify the mechanism of alteration by high temperature. As a representative, Taylor summarized the alteration mechanisms at a specified temperature as follows [1]; free water evaporates between 30 °C and 100 °C, and loss of chemically-bound water in the C-S-H and carboaluminate hydrates between 180 °C and 300 °C. From 450 °C and 550 °C, calcium hydroxide decomposes into calcium oxide. Finally, calcium carbonate and C-S-H gel begin to decompose between 600 °C and 700 °C. In other past studies, Mendes et al. [2] revealed that the critical temperature for OPC pastes was 400 °C because above this temperature OPC pastes cause dehydration of calcium hydroxide and rehydration of calcium oxide. Many researchers conducted the experiment around this temperature and discussed the presence or absence of calcium hydroxide [3-5]. On the other hand, Castellote et al. monitored the decomposition of calcium hydroxide between 530 and 560 °C by neutron diffraction in powder and bulk samples [6]. (✓)

Thus, the thermal decomposition of cement hydration is still unclear. Some of the reasons can be considered as the difference of experimental conditions, such as heating conditions, the state of sample (bulk or powder), and so forth. As for the state of sample, the bulk one is closer to actual conditions in service environment. Therefore, the technique that can grasp the internal structure in non-destructive manner is more effective way to analyze the alteration progress of concrete.

In previous researches concerning alteration mechanism by high temperature, there still exists a lack of studies considered as followings. (✓)

While concrete structures may suffer from high temperature like a fire event during their long service life, many research did not considered the effect of carbonation. Carbonation is mechanically beneficial by clogging the bigger capillary pores and refining the microstructure [7]. This should surely affect the properties of concrete after exposure of high temperature. (✓)

Moreover, re-curing fire-damaged concrete in water or a high humidity environment can lead to performance recovery and it is suggested that water supply on fire damaged concrete is an environmental and economic procedure to recover its strength [8, 9]. On the other hand, it is concerned that volume increase with the reaction may reduce performance due to the expansion of cracks [10]; therefore, the effect of re-curing is still unclear.

This study aims to investigate the effect of carbonation on high temperature alteration behavior and the change of microstructure of fire-damaged concrete before and after immersion in pure water by using newly micro-tomographic method called non-destructive integrated CT-XRD method [11]. Powder X-Ray diffraction (XRD) was conventionally utilized to identify the cement hydration system before and after heating [12, 13]. However, this methodology is destructive and thus limits the ability to understand the change of microstructure over time and consider properly the internal state of concrete like moisture due to grind process. On the other hand, X-ray Computed

1 Tomography (CT) is useful to analyze internal microstructure three-dimensionally and
2 recently utilized by various researches in cement and concrete field [14-17]. However,
3 even using a synchrotron radiation X-ray source, it is difficult to detect the distribution
4 of minerals in a cement hydrated system, which means only CT images with lower
5 contrast can be obtained because of small differences in the linear attenuation coefficient
6 of minerals in a cement hydrated system. To solve this problem, our research group found
7 out the advantage of coupling CT and XRD measurement and started the development
8 and application of non-destructive integrated CT-XRD method (hereafter the CT-XRD).
9 Simultaneously, modification to improve the image quality in CT measurement and
10 signal ratio in XRD measurement were carried out and some accomplished by changing
11 the arrangement of the equipment. Although various improvements of the system are still
12 going on, this method clarified the leaching behavior in the vicinity of crack of
13 cementitious materials due to water flow [18], and this led to the motivation to apply the
14 alteration behavior due to high temperature. In this paper, an attempt to do so was carried
15 out and the obtained results were discussed.

17 **2. Experimental program**

19 An overview of the experimental program is shown in Fig. 1. Two types of experiments
20 were carried out; one is the CT-XRD measurement followed by Powder X-ray diffraction
21 measurement using carbonated or non-carbonated samples (Experiment I) and the other
22 is to investigate the effect of immersion in deionized water on fire-damaged cementitious
23 material (Experiment II).

25 **2.1. Sample preparation**

26 Cement paste with only the Ordinary Portland Cement was used in both experiments. A
27 water to cement ratio is 0.6. The cement paste was mixed and molded into metal frame in
28 the size of 40×40×160 mm. The samples were de-molded after 24 hours of molding, and
29 then cured in tap water until cutting. After about 12 months of water-curing, the hardened
30 cement pastes were cut into the prism in the size of 2.5×2.5×5 mm for the CT-XRD
31 measurement. Carbonation test and heating test described in the next section were carried
32 out followed by setting the samples on the jig using epoxy resin. Hereafter, the non-
33 carbonated samples and carbonated samples are described as N and C, respectively.

34 **2.2. Testing**

35 **2.2.1. Carbonation test**

36 Before the CT-XRD measurement in both Experiment I and II, samples were carbonated
37 doing the following procedure; samples were left in a container inside constant
38 temperature furnace under 100 °C condition. 99% CO₂ gas was injected into the
39 container per 1 day and this process was continued for a period of 7 days.

40 **2.2.2. Heating test**

41 Heating test was carried out using electric furnace with a temperature control program in
42 both Experiment I and II. The rate of heat increase was set at 10 °C per minute until the
43 target maximum temperature was reached. The maximum temperature was maintained
44 for 2 hours and the rate of heat decrease was also set at 10 °C per minute until room
45 temperature. The target maximum temperature was 200, 400, 600, and 800 °C denoted
46 by 2, 4, 6 and 8, and Non-Heated (NH) sample was also prepared.

47 **2.2.3. Immersion test**

1 After the heating test and initial CT-XRD measurement in Experiment II, samples were
2 immersed into deionized water. Immersion test was continued for a period of 28 days,
3 with change of water every 7 days. The samples before immersion and after immersion
4 are denoted by B and A, respectively.

5 **2.3. Non-Destructive Integrated CT-XRD Method**

6 **2.3.1. Outline**

7 The CT-XRD has been developed at BL28B2 in the synchrotron radiation facility,
8 SPring-8 (Super Photon ring-8GeV), in Japan [19-21]. The BL28B2 has powerful white
9 X-ray source which can be currently available. White X-ray covers a wide range of wave
10 length zone. Therefore, with using a white X-ray as the incident X-ray there is no need to
11 scan the angle between sample and detector, and energy-dispersive XRD profile can be
12 obtained. Fig. 2 shows the outline of this method.

13 **2.3.2. CT measurement**

14 White X-ray is emitted to a silicon mono-crystal located in upstream position of sample
15 and then diffracted to a specific angle with getting itself monochromatic as shown in Fig.
16 2. Sample is set in the direction of diffracted X-ray and exposed followed by capture of
17 X-ray camera. The reason why the monochromatic X-ray extracted from the white X-ray
18 is used for the enhancement of image contrast. Therefore, the couple of CT and XRD
19 measurement is applicable using same X-ray source. The stage that sample sets is
20 revolving during CT measurement and thus transmission images of X-ray with different
21 angles can be obtained. Image reconstruction can be carried out by back projection of the
22 transmission images. The reconstructed images in three dimensions can be referred as
23 determinations of ROI followed by XRD measurement.

24 **2.3.3. XRD measurement**

25 X-ray diffraction profile can be obtained in the Region of Interest (ROI). Sample is moved
26 on the straight line of X-ray irradiating direction as shown in Fig. 2. In order to extract
27 the signal of the X-ray diffraction only in the ROI, three slits are deployed in the system.
28 A slit in the upstream position (S1) and two slits in the downstream (S2 and S3) are
29 installed so as to focus a specific space and obtain the only signals of X-ray diffraction
30 there, called the gauge volume. The gauge volume can be set on ROI because the
31 coordinate system in the CT measurement corresponds to that in the XRD measurement.
32 A solid-state detector is used and located behind S2 and S3. The angle of the arm that
33 corresponds to the twice of the diffraction angle (2θ) is fixed at 10° during the
34 measurement and the relationship between X-ray energy and the intensity of diffracted
35 X-ray can be obtained.

36 **2.3.4 Setup conditions**

37 Setup conditions in this measurement are followings; the extracted energy of X-ray CT
38 measurement was 25 keV. Angle steps during CT measurement were 0.12° with an
39 exposure time of 0.4 s. Image resolution was $2.44 \mu\text{m}/\text{voxel}$. The beam size was 0.05 mm
40 in width and 0.3 mm in height. The angle of diffraction (θ) was fixed at 5° and the preset
41 time was 300 s.

42 **2.4. Powder X-ray Diffraction**

43 Powder X-ray diffraction (P-XRD) was used to identify the crystalline phases of the
44 cement paste and verify the data from the CT-XRD in Experiment I. Samples were
45 grinded into powder in a diameter of less than $100\mu\text{m}$ and P-XRD measurement was
46 carried out soon after grinding. XRD data were recorded using SmartLab produced by
47 Rigaku. The scanning range was $2\theta = 10^\circ$ to 60° degrees with a 0.01 step scan and a

1 scanning speed of 5.5 degrees per minute. The diffraction profile was acquired and
2 analyzed using powder diffraction analysis software “PDXL” from Rigaku.
3 To compare the results of the CT-XRD and Powder-XRD, the variable number, “Energy”
4 from the CT-XRD results, was converted to “diffraction angle” using two relationships;
5 one is the relationship of light and energy (see (1)) and the other is Bragg’s equation (see
6 (2)).
7

$$8 \quad E = \frac{hc}{\lambda} = \frac{12.3983}{\lambda} \quad (1)$$

9
10 Where E is the energy of incident X-ray, h is the planck constant ($\doteq 6.63 \times 10^{-34}$), c is the
11 speed of light ($\doteq 3.00 \times 10^8$), and λ is the wavelength of the incident wave.
12

$$13 \quad \lambda = 2d \sin \theta \quad (2)$$

14
15 Where d is the spacing between the planes, and theta is the angle between the incident X-
16 ray and the scattering planes.
17

18 **3. Results and Discussions**

19
20 The ROI was set in the center of each sample, which consists of continuous 300 slices, as
21 shown in Fig. 3. With stacking up all slices, a 3D image in the scanning area can be
22 obtained. Image processing was carried out by using free software “ImageJ” [22] and
23 public domain program “SLICE” [23].
24

25 **3.1. Experiment I**

26 **3.1.1. CT measurement**

27 Fig. 4 shows micro-tomographic images of each sample. The cross section is located in
28 the middle height of sample. CT images are typically represented in the gray scale (GSV).
29 Therefore, images have two areas; light grey indicates the cement paste and dark color
30 represents air, voids, and crack. Each slice was processed a matrix size into 1280×1280
31 pixels. According to N-series, the images show that some cracks were observed in N-4
32 and more cracks clearly can be seen in N-6 and N-8. As for C-series, only C-8 has
33 significant cracks. Cracks were formed from the outer edge into the center. It can be
34 inferred that the decomposition of portlandite started to occur higher than 400°C and
35 triggered the cracking in N-series. In addition, calcite or C-S-H decomposed in C-series
36 at 800 °C, which may result in cracking. This is discussed in the next section.
37

38 **3.1.2. XRD measurement**

39 ROIs were determined for XRD measurements as Point 1 to Point 3 from the corner to
40 the center (shown as circle in Fig. 4). Fig. 5 shows an example of series of XRD profiles
41 (C-NH); P-XRD, Point 1, Point 2, and Point 3 are shown from top to bottom. It can be
42 found from P-XRD profile that, the peaks of calcite are distinct whereas some peaks of
43 portlandite can be seen. Moreover, small peaks of vaterite also can be found. Groves et
44 al. [24] observed calcium carbonate is formed mainly in outer product regions of C-S-H
45 as microcrystalline vaterite and calcite, and residual portlandite embedded in vaterite is
46 also observed using TEM. This is the reason why the peaks of vaterite were also detected.
47 A small peak of belite was also detected, which is derived from the presence of
anhydrated cement phases.

1 With regard to the profile of Point 1, the peaks of calcite are distinct and a peak of belite
2 is also confirmed. On the other hand, the peaks of portlandite cannot be found. On the
3 other hand, profiles of Point 2 and Point 3 exhibit that the peaks of portlandite are distinct
4 whereas the peaks of calcite are very weaker than that of Point 1. These profiles reveal
5 that carbonation progressed at the surface layer due to the reaction of atmospheric CO₂
6 and portlandite. The presence of belite is also derived from anhydrous cement particles.
7 Comparison with P-XRD and the CT-XRD indicates that there is a limitation for the CT-
8 XRD to observe peaks in the range of less than 25° or less. This may derive from
9 absorption of X-ray in low energy range. Moreover, the peaks of the CT-XRD is broader
10 than those of P-XRD, thus closer peaks cannot be shown separately, represented as the
11 range of 45° and 50°. However, the peak positions can be correctly shown in the profiles
12 of the CT-XRD. Therefore, the CT-XRD can evaluate the effect of alteration (carbonation
13 in this case) in non-destructive manner.

14 Crystal phases identified by the CT-XRD for each point are shown in Table 1. With regard
15 to portlandite, no peaks can be seen in Point 1. Thus, carbonation occurred at the surface
16 layer in contact with CO₂. Its decomposition observed at higher than 600°C. The peaks
17 can be detected in Point 2 and Point 3 of N-6 whereas no peaks are shown in P-XRD.
18 Castellote et al. [6] revealed that portlandite with less crystalline was reformed due to the
19 reaction of lime with water vapor when cooling procedure. Therefore, it can be considered
20 that this reaction occurred inside the sample due to the presence of moisture like free
21 water. In addition, Scrivener et al. [25] pointed out that the friction during intense
22 grinding processes in preparing the powder sample may cause loss of crystal water and
23 changes in the phase assemblage. Thus, the less crystalline structure was easily destroyed
24 during grinding procedure. The profiles of C-6 have no peaks of portlandite, which
25 indicates that reformation of portlandite did not occur. It might be because of shortage of
26 free water evaporated at carbonation test.

27 According to calcite, the peaks can be detected in P-XRD or Point 1 for N-series except
28 N-8, which derives from much contact with air-induced CO₂. C-NH was carbonated up
29 to Point 2. C-2, C-4, and C-6 were carbonated up to Point 3. Ref. [26] indicated that
30 carbonation depth is proportional to elevated temperature, which supports the results in
31 this research. The profiles of N-8 and C-8 in the CT-XRD have the peak of lime while P-
32 XRD has the peaks of calcite. This fact indicates that the reaction of lime with CO₂ in air
33 progressed rapidly because the hydration was not stopped beforehand.

34 vaterite was observed less than 400°C. It is known that vaterite transforms to calcite
35 around 500 °C [27], which confirms this result.

36 Alite and belite was detected mostly in N-8 and C-8. It can be considered that these
37 products were derived from the decomposition of C-S-H, being consistent with previous
38 researches [28, 29].

39 Throughout the XRD results in this experiment, it can be concluded that the CT-XRD has
40 a strong feature that can identify the crystals of internal structure properly, as symbolized
41 in N-6.

42 **3.2. Experiment II**

43 **3.2.1. CT measurement**

44 Fig. 6 shows cross sectional images of each sample resulted from Experiment II. The
45 cross section is located in the middle height of sample. Each slice was processed a matrix
46 size into 1500×1500 pixels. With regard to the images before immersion, cracks can be
47 seen only in the C-8, which is same as Experiment I. It can confirm that the cracks
48 generated due to decomposition of calcite at higher than 600°C. However, the images

1 after immersion indicate that the edge became porous in C-NH, C-2, and C-4. Moreover,
2 the edge of C-6 sample becomes more porous than these three samples and that of C-8
3 sample becomes darker. It derived from calcium leaching due to immersion and
4 maximum temperature before immersion affected the degree of leaching.

5 Fig. 7 shows the CT histogram of Linear Attenuation Coefficient (LAC) of NH sample
6 before immersion and example of rescaling to 8bit gray scale image. There are two
7 distinct peaks which are associated with the air and the cement matrix, respectively. From
8 Fig. 7, it can be said that larger peaks position around the value of 4.8 before immersion.
9 Table 2 provides the list of some of the referred minerals for hardened cement pastes with
10 LAC at the X-ray energy level of 25 keV. LAC of the referred minerals was obtained
11 from the NIST database [30] after inputting the chemical compounds and density of
12 targeted mineral, which was referred to Ref. [31-33]. According to this table, the larger
13 peak is closer to the LAC of C-S-H-I and other candidate minerals like portlandite can be
14 negligible. Therefore, it can be said that the area of cement paste in cross sectional images
15 mainly indicates the distribution of C-S-H. In addition, in order to enhance the contrast
16 and process the images easily, rescaling images was carried out. In this study, all the CT
17 images were consistently converted to 8bit gray scale images by setting the minimum and
18 maximum to -2 and 8, respectively. Fig.8 shows the histograms of each sample in 8bit
19 scale and the way to determine the thresholds. Compared with histograms before and after
20 immersion, the peak of cement paste in C-NH, C-2, and C-4 shifted slightly to lower
21 values than that of before immersion. Moreover, it can be said that the peak of cement
22 paste in 600°C and 800°C was separated into two peaks. These shifts can be discussed as
23 followings.

24 Saito et al. showed the conceptual diagram of calcium leaching evaluated by an
25 electrochemical technique, as shown in Fig. 9 [34]. It indicates that the states of cement
26 matrix can be expressed as four phases; Only SiO₂ exists in phase 1; C-S-H with
27 decreased C/S ratio remains in phase 2; C-S-H with high C/S ratio exists in phase 3; both
28 C-S-H and portlandite (CH) remains in phase 4. According to this diagram, obtained CT
29 images can be confirmed that; phase 1 is shown represented in the edge of C-8, phase 2
30 is shown represented in the edge of C-6, and both phase 3 and phase 4 are shown
31 represented in the center of all samples. Phase 3 and phase 4 are not distinctive from the
32 CT measurement because the peak of portlandite was not shown in histogram. Each
33 threshold was determined to select the point of intersection in C-6-A and C-8-A.
34 Threshold of air and Phase 1 is 82, the intersection between the right end of air peak and
35 GSV axis in C-6-A. That of Phase 1 and Phase 2 is 130, the intersection between profile
36 of C-6-A and C-8-A, and that of Phase 2 and Phase 3 was determined 155, the intersection
37 between the first peak and second peak in the profile of C-6-A. Total leaching area could
38 be extracted from the CT images dependent on these thresholds, segmented air as black,
39 phase 1 as red, phase 2 as green and phase 3 and 4 as white color.

40 Fig. 10 shows the segmented images of each sample. First, it can be seen that leaching
41 effect was observed equally from edge to center but blocked in some side of C-2 and C-
42 6 sample. This might be derived from attaching epoxy on the side of samples accidentally
43 when attaching themselves to jigs. From segmented images, leaching front was measured
44 by drawing arbitrary 4 points on images and then taking average of them. Fig. 11 shows
45 the leaching front for each sample. According to this graph, C-4 exhibited the smallest
46 leaching front of 0.1mm. This might be because of the fact that the clogging of the whole
47 range of pores by the carbonation test [35]. After that, heating procedure produced so-
48 called condition of internal autoclaving in cement paste [36]. This is particularly true for

1 dense cement paste because low permeability resists moisture flow [37]. Therefore,
2 additional hydration of unhydrated cement grains occurred effectively and thus increased
3 the resistance of leaching in C-4 sample more than C-NH. A comparison of other samples
4 showed that C-NH and C-2 resulted in 0.34 mm in leaching depth, and leaching depth of
5 C-6 became deeper, 0.41mm including increased phase 1. The surface of C-8 altered to
6 phase 1 mostly, and the depth is 0.44mm.

7 8 **3.2.2. XRD measurement**

9 Regions of interests were determined for XRD measurements as point 1 to point 4 from
10 the corner to the center (shown in Fig. 6 as circle).

11 Fig. 12 shows the XRD profiles of each sample before and after immersion test for the
12 Point 1 to Point 4. With regard to C-NH, the peaks of both portlandite and calcite can be
13 seen at all points before immersion and the peaks of portlandite disappeared after
14 immersion. It indicates that portlandite dissolved into water from all area. The weakened
15 peaks of portlandite were observed in the profile of Point 3 and 4 after immersion in the
16 profiles of C-2. Moreover, in case of C-4, those were still observed in that of Point 2, 3
17 and 4, which corresponds to smaller leaching front in Fig. 11. Therefore, these results
18 confirmed the increase of resistance against leaching under the influence of elevated
19 temperatures up to 400 °C. The profiles of C-6 show that almost all no change can be
20 seen before and after immersion and the peaks of calcite can be detected and the peaks of
21 portlandite cannot be detected. As indicated in Figure 11, the leaching front became
22 deeper at 600 °C or more. Thus, the initial presence or absence of portlandite affected
23 rapid dissolution of C-S-H. Concerning the profiles of C-8, the peaks of alite and belite
24 were found clearly before immersion at all points. It was considered that these
25 productions derived from the decomposition of C-S-H. After immersion, however, the
26 peaks of portlandite can be seen at Point 3 and 4 and only tiny peaks of calcite and belite
27 were observed at Point 1 and 2. Moreover, the peaks of alite and belite disappeared at all.
28 These indicate that clinker-based minerals were rehydrated to produce portlandite in all
29 depth meanwhile the dissolution of the portlandite produced by the rehydration occurred
30 in Point 1 and Point 2.

31 32 **4. Conclusion**

33 Based on this research, conclusions are summarized as follows.

- 34 (1) Regardless of limitation to detect the intensity peaks in the range of less than 25° and
35 adjacent peaks separately, non-destructive integrated CT-XRD method can evaluate
36 the peak positions and thus evaluate alteration of internal structure in non-destructive
37 manner.
- 38 (2) In the cement paste heated at 600°C, the presence of portlandite was observed in the
39 profile of the CT-XRD. It can be considered that the portlandite was reformed during
40 cooling. However, its formation was hardly observed in the profile of Powder XRD.
41 Hence the portlandite with less crystalline nature might be destroyed in the process
42 of the grinding to prepare the powder.
- 43 (3) CT image analysis revealed that the cement paste that was carbonated and then heated
44 at 400°C exhibited the largest resistance against leaching in water immersion. It
45 appeared to be due to the densification of the internal structures.
- 46 (4) While alite and belite were generated in the cement paste due to heating at 800°C
47 they could rehydrate themselves and form portlandite by immersion in pure water.

1 Subsequently, however, its dissolution occurred at the surface layer and the structure
2 of cement hydration system became the most coarsened.

3 4 **Acknowledgment**

5
6 This research was partially supported by the Japan Society for the Promotion of Science
7 (JSPS KAKENHI grant number 17J01145). The synchrotron radiation experiments were
8 performed at the BL28B2 beamline at SPring-8 with the approval of the Japan
9 Synchrotron Radiation Research Institute (JASRI) (Proposal No. 2012B1282,
10 2013B1511, 2014A1559, 2014B1010, 2015A1002, 2015B1569, 2015A1532,
11 2016A1532, 2017A1009, 2017B1021, 2018A1565, 2018A1691, 2018B1017). The
12 authors would like to thank Dr. T. Hitomi (Obayashi Co.) and Dr. K. Kajiwara (JASRI)
13 for their assistance in the experiment.

14 15 16 **References**

- 17
18 [1] Taylor, H.F.W. (1997). “*Cement Chemistry*.” London: Academic Press.
19
20 [2] Mendes, A., Sanjayan, J. G., and Collins, F. (2009). “Long-term progressive
21 deterioration following fire exposure of OPC versus slag blended cement pastes.”
22 *Materials and Structures*, 42(1), 95-101.
23
24 [3] Handoo, S. K., Agarwal, S., and Agarawal, S. K. (2002). “Physicochemical,
25 mineralogical, and morphological characteristics of concrete exposed to elevated
26 temperatures.” *Cement and Concrete Research*, 32(7), 1009-1018.
27
28 [4] Alonso, C., and Fernandez, L. (2004). “Dehydration and rehydration processes of
29 cement paste exposed to high temperature environments.” *Journal of Materials Science*,
30 39(9), 1009-1018.
31
32 [5] Wang, G., Zhang, C., Zhang, B., Li, Q, and Shui, Z. (2015). “Study on the high-
33 temperature behavior and rehydration characteristics of hardened cement paste.” *Fire and*
34 *Materials*, 39(8), 741-750.
35
36 [6] Castellote, M., Alonso, C., Andrade, C., Turrillas, X., and Campo, J. (2004).
37 “Composition and microstructural changes of cement pastes upon heating, as studied by
38 neutron diffraction.” *Cement and Concrete Research*, 34(9), 1633-1644.
39
40 [7] Pihlajavaara, S. E. (1968). “Some results of the effect of carbonation on the porosity
41 and pore size distribution of cement paste.” *Materials and Constructions*, 1(6), 521-527.
42
43 [8] Poon, C., Azhar, S., Anson, M., and Wong, Y. L. (2001) “Comparison of the strength
44 and durability performance of normal and high strength pozzolanic concretes at elevated
45 temperatures.” *Cement and Concrete Research*, 31(9), 291-300.
46

- 1 [9] Lin, Y., Hsiao, C., Yang, H., and Lin, Y. F. (2011). "The effect of post-fire-curing on
2 strength-velocity relationship for nondestructive assessment of fire-damaged concrete
3 strength." *Fire Safety Journal*, 46(4), 178-185.
4
- 5 [10] Lin, W-M., Lin, T. D., and Powers-Couche, L. J. (1996) "Effect of fire-damaged
6 concrete." *ACI Materials Journal*, 93(3), 199-205
7
- 8 [11] Sugiyama, T., Hitomi, T. and Kajiwara, K. (2014). "Nondestructive Integrated CT-
9 XRD Method for Research on Hydrated Cement System." *Proceedings of the 4th*
10 *International Conference on the Durability of Concrete Structures*, 298-303.
11
- 12 [12] Ibrahim, R. K., Hamid, R., and Taha, M. R. (2012). "Fire resistance of high-volume
13 fly ash mortars with nanosilica addition." *Construction and Building Materials*, 36, 779-
14 786.
15
- 16 [13] Wang, S. G., Zhang, C., Zhang, B., Li, Q., and Shui, Z. (2015). "Study on the high-
17 temperature behavior and rehydration characteristics of hardened cement paste." *Fire and*
18 *Materials*, 39(8), 741-750.
19
- 20 [14] Gallucci, E., Scrivener, K., Groso, A., Stampanoni, M., and Margaritondo, G. (2007).
21 "3D experimental investigation of the microstructure of cement pastes using synchrotron
22 X-ray microtomography." *Cement and Concrete Research*, 37(3), 360-368.
23
- 24 [15] Promentilla, M. A. B., Sugiyama, T., Hitomi, T., and Takeda, N. (2009).
25 "Quantification of tortuosity in hardened cement pastes using synchrotron-based-X-ray
26 computed microtomography." *Cement and Concrete Research*, 39(6), 548-557.
27
- 28 [16] Sugiyama, T., Promentilla, M. A. B., Hitomi, T., Takeda, N. (2010). "Application of
29 synchrotron microtomography for pore structure characterization of deteriorated
30 cementitious materials due to leaching." *Cement and Concrete Research*, 40(8), 1265-
31 1270.
32
- 33 [17] Henry M., Hashimoto, K., Ivan, S. D., and Sugiyama, T. (2016) "Cracking and
34 chemical composition of cement paste subjected to heating and water re-curing." *Journal*
35 *of Advanced Concrete Technology*, 14(4), 134-143.
36
- 37 [18] Takahashi, H., and Sugiyama, T. (2016). "Investigation of alteration of deteriorated
38 mortar due to water attack using non-destructive integrated CT-XRD method." *Proceedings of the 11th fib International Ph.D Symposium in Civil Engineering*, 445-452.
39
40
- 41 [19] Hitomi, T., Kajiwara, K., and Sugiyama, T. (2013). "Micro-observation of chemical
42 compounds in mortar by non-destructive integrated CT-XRD method." *The Proceedings*
43 *of 67th Annual Convention of Japan Cement Association*, 80-81 (in Japanese).
44
- 45 [20] Kajiwara, K., Hitomi, T., and Sugiyama, T. (2013). "Development of non-
46 destructive integrated CT-XRD method for the evaluation of mineral distribution in
47 cementitious materials." *The Proceedings of 67th Annual Convention of Japan Cement*
48 *Association*, 82-83 (in Japanese).

1
2 [21] Ikeda, S., Sugiyama, T., Hitomi, T., and Kajiwara, K. (2013). “Non-destructive
3 integrated CT-XRD method for the observation of alteration of hardened cement paste
4 with cracks due to water flow.” *The Proceedings of 67th Annual Convention of Japan
5 Cement Association*, 84-85 (in Japanese).

6
7 [22] Rasband, W. (2007). ImageJ: Image processing and analysis in Java, National
8 Institute of Health (NIH). Available from: <<http://rsb.info.nih.gov/ij/>>.

9
10 [23] Nakano, T., Tsuchiyama, A., Uesugi, K., Uesugi, M., and Shinohara, K. (2006).
11 “SLICE –Software for basic 3-D image analysis [online].” Japan Synchrotron Radiation
12 Research Institute (JASRI). Available from: <<http://www-bl20.spring8.or.jp/slice/>>.

13
14 [24] Groves, G. W., Rodway, D. I., and Richardson, I. G. (1990). “The carbonation of
15 hardened cement pastes.” *Advances in Cement Research*, 3(11), 117-125.

16
17 [25] Scrivener, K., Snellings, R., and Lothenbach, B. (2016). “A practical guide to
18 microstructural analysis of cementitious materials.” Boca Raton: CRC Press.

19
20 [26] Li, Z., and Li, Q. (2011). “Experimental investigation on property recovery of
21 concrete exposed to high temperature.” *Journal of Structural and Construction
22 Engineering*, 76(666), 1375-1382 (in Japanese).

23
24 [27] Rao, M. S. (1973). “Kinetics and mechanism of the transformation of vaterite to
25 calcite.” *Bulletin of the Chemical Society of Japan*, 46(5), 1414-1417.

26
27 [28] Piasta, J. Sawics, Z. and Rudzinski, L. (1984). “Changes in the structures of hardened
28 cement paste due to high temperatures.” *Materials and Structures*, 17(4), 291-296.

29
30 [29] Peng, G, F. and Huang, Z, S. (2008). “Changes in microstructure of hardened cement
31 subjected to elevated temperatures.” *Construction and Building Materials*, 22(4), 593-
32 599.

33
34 [30] Chantler, C. T., Olsen, K., Dragoset, R. A., Chang, J., Kishore, A.R., Kotochigova,
35 S. A., and Zucker, D.S. (2005). “X-ray Form Factor, Attenuation, and Scattering Tables
36 (version 2.1.) [online].” National Institute of Standards and Technology, Gaithersburg,
37 MD, Available from: <<https://physics.nist.gov/PhysRefData/FFast/>> [08 Aug. 2018].

38
39 [31] Bentz, D. P., Coveney, P. V., Garboczi, E. J., Kleyn, M. F., and Stutzman, P. E.
40 (1994). “Cellular automaton simulations of cement hydration and microstructure
41 development.” *Modelling and Simulation in Material Science and Engineering*, 2, 783-
42 808.

43
44 [32] Allen, A. J., Thomas, J. J., and Jennings, H. M. (2007). “Composition and density of
45 nanoscale calcium-silicate-hydrate in cement.” *Nature Materials*. 6(4), 311-316.

46
47 [33] Balonis, M. and Glasser, F. P. (2009). “The density of cement phases.” *Cement and
48 Concrete Research*, 39(9), 733-739.

1
2
3
4
5
6
7
8
9
10
11
12
13
14
15
16
17
18
19
20
21
22
23
24
25
26
27
28
29
30
31
32
33
34
35
36
37
38
39
40
41
42
43
44
45
46
47
48

[34] Saito, H., Tsuji, Y., and Kataoka, H. (2000). "A Model for Predicting the Leaching Degradation of Cement Hydrate." *Concrete Research and Technology*, 11(1), 51-59 (in Japanese).

[35] Morandau, A., Thiery, M., and Dangla, P. (2015) "Impact of accelerated carbonation on OPC cement paste blended with fly ash." *Cement and Concrete Research*, 67, 226-236.

[36] Saad, M., Abo-El-Enein, S. A., Hanna, G. B., Kotkata, M. F. (1996). "Effect of temperature on physical and mechanical properties of concrete containing silica fume." *Cement and Concrete Research*, 26(5), 669-675.

[37] Ma, Q., Guo, R., Zhao, Z., Lin, Z., and He, K. (2015). "Mechanical properties of concrete at high temperature-A review." *Construction and Building Materials*, 93, 371-383.

1	List of Tables
2	
3	Table 1 Crystal phase for each sample identified by both P-XRD and the CT-XRD
4	
5	Table 2 Composition, notation, density, and linear attenuation coefficient of different
6	phases
7	
8	List of Figures
9	
10	Figure 1 Overview of experimental program
11	
12	Figure 2 Schematic diagram of the system for non-destructive integrated CT-XRD
13	method
14	
15	Figure 3 Image analysis area in CT measurement
16	
17	Figure 4 Cross sectional images at center heights in Experiment I. The markers indicate
18	the position of XRD measurement
19	
20	Figure 5 XRD profiles of C-NH by P-XRD (P) and the CT-XRD (1, 2, and 3)
21	(alite:▲, belite:○, portlandite:■, calcite:□, vaterite:◆, lime:●)
22	
23	Figure 6 Cross sectional images at center heights in Experiment II. The markers indicate
24	the position of XRD points
25	
26	Figure 7 Example of CT histogram of the CT images and rescaling to 8bit gray scale
27	images [#2(6)]
28	
29	
30	Figure 8 Histograms of each sample before and after immersion and threshold
31	determination for phase segmentation
32	
33	Figure 9 Schematic diagram of alteration mechanism with calcium leaching (revised Ref.
34	[33])
35	
36	Figure 10 Region of Interest extracted from original data set and visualization of leaching
37	area from phase segmentation (colored as phase 1 in red, phase 2 in green, and phase 3 &
38	4 in white)
39	
40	Figure 11 Leaching front for each sample measured from segmented images
41	
42	Figure 12 XRD profiles of all samples before and after immersion by the CT-XRD (1, 2,
43	3, and 4) (alite:▲, belite:○, portlandite:■, calcite:□, vaterite:◆, lime:●)
44	
45	
46	
47	
48	

1 Table 1 The crystal phase for each sample identified by both P-XRD and the CT-XRD
 2

Sample		Portlandite				Calcite				Vaterite				Alite				Belite				P
		P	1	2	3	P	1	2	3	P	1	2	3	P	1	2	3	P	1	2	3	
N	NH	○	×	○	○	○	○	×	×	○	○	×	×	×	×	×	×	△	△	×	×	△
	2	○	×	○	○	○	○	×	×	○	△	×	×	×	×	×	×	△	△	×	×	△
	4	○	×	○	○	○	○	×	×	○	○	×	×	×	×	×	×	△	△	×	×	△
	6	×	×	○	○	○	○	×	×	×	×	×	×	×	×	×	×	△	△	×	×	△
	8	×	×	×	×	○	×	×	×	×	×	×	×	○	○	○	○	○	○	○	○	○
C	NH	○	×	○	○	○	○	○	×	○	×	×	×	×	×	×	×	△	△	×	×	△
	2	○	×	○	○	○	○	○	○	○	○	×	×	×	×	×	×	△	△	×	×	△
	4	○	×	○	○	○	○	○	○	○	×	×	×	×	×	×	×	△	△	×	×	△
	6	×	×	×	×	○	○	○	○	×	×	×	×	×	×	×	×	△	△	△	△	△
	8	×	×	×	×	○	×	×	×	×	×	×	×	○	○	○	○	○	○	○	○	○

3
 4
 5
 6
 7
 8
 9
 10
 11
 12
 13
 14
 15
 16
 17
 18
 19
 20
 21
 22
 23
 24
 25
 26
 27
 28 Table 2 Composition, notation, density, and linear attenuation coefficient of different
 29 phases

1

Phase	Chemica Formula	Notation	Density	Linear Attenuation Coefficient at 25 keV
Ferrite	$(\text{CaO})_4(\text{Al}_2\text{O}_3)(\text{Fe}_2\text{O}_3)$	C_4AF	3.708	21.21
Free lime	CaO	C	3.341	16.67
Alite	$(\text{CaO})_3(\text{SiO}_2)$	C_3S	3.120	12.59
Belite	$(\text{CaO})_2(\text{SiO}_2)$	C_2S	3.326	12.40
Aluminate	$(\text{CaO})_3(\text{Al}_2\text{O}_3)$	C_3A	3.030	11.27
Anhydrite	CaSO_4	CS	2.968	9.28
Portlandite	$\text{Ca}(\text{OH})_2$	CH	2.251	8.79
Calcite	CaCO_3	C	2.710	8.14
Calcium Silicate Hydrate (Jennnite)	$(\text{CaO})_9(\text{SiO}_2)_6 \cdot 11\text{H}_2\text{O}$	CSH	2.331	6.83
Calcium Silicate Hydrate (Tobermorite 14Å)	$(\text{CaO})_5(\text{SiO}_2)_6 \cdot 8\text{H}_2\text{O}$	CSH	2.228	5.58
Calcium Silicate Hydrate (Afwillite)	$(\text{CaO})_3(\text{SiO}_2)_2 \cdot 3\text{H}_2\text{O}$	CSH	2.645	7.97
Calcium Silicate Hydrate I	$(\text{CaO})_{1.7}(\text{SiO}_2)4\text{H}_2\text{O}$	CSH	1.85 ^{a)}	4.83
Calcium Silicate Hydrate II	$(\text{CaO})_{1.7}(\text{SiO}_2)1.8\text{H}_2\text{O}$	CSH	2.604 ^{b)}	8.58
Gypsum	$\text{CaSO}_4 \cdot 2\text{H}_2\text{O}$	CSH_2	2.311	5.89
Monosulfate	$(\text{CaO})_3(\text{Al}_2\text{O}_3)(\text{CaSO}_4)12\text{H}_2\text{O}$	$\text{C}_4\text{ASH}_{12}$	2.015	4.21
Periclase	MgO	M	3.584	3.91
Quartz	SiO_2	S	2.641	3.62
Ettringite	$(\text{CaO})_3(\text{Al}_2\text{O}_3)(\text{CaSO}_4)_3 \cdot 32\text{H}_2\text{O}$	$\text{C}_6\text{ASH}_{32}$	1.778	3.56

2 Sources: a) Bentz et al. (1994); b) Allen et al. (2007);

3 no mark) Balonis and Glasser (2009)

4

5

1
2
3
4
5
6
7

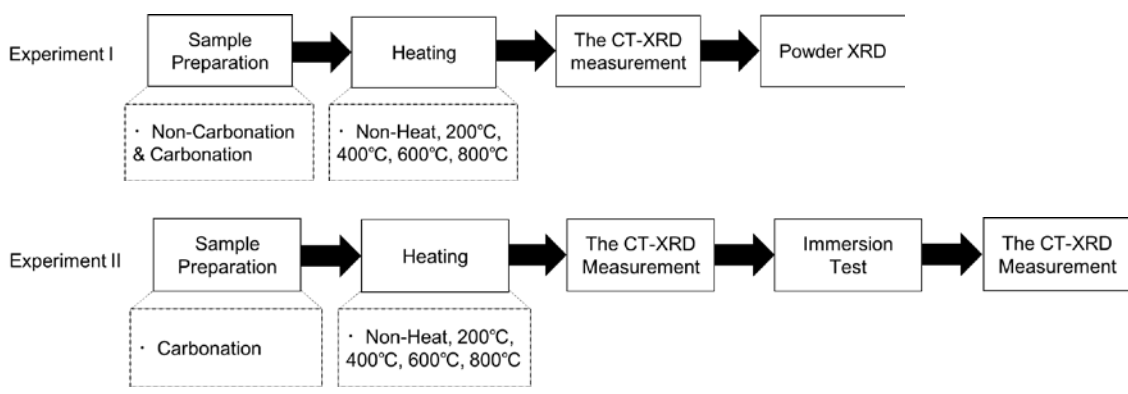
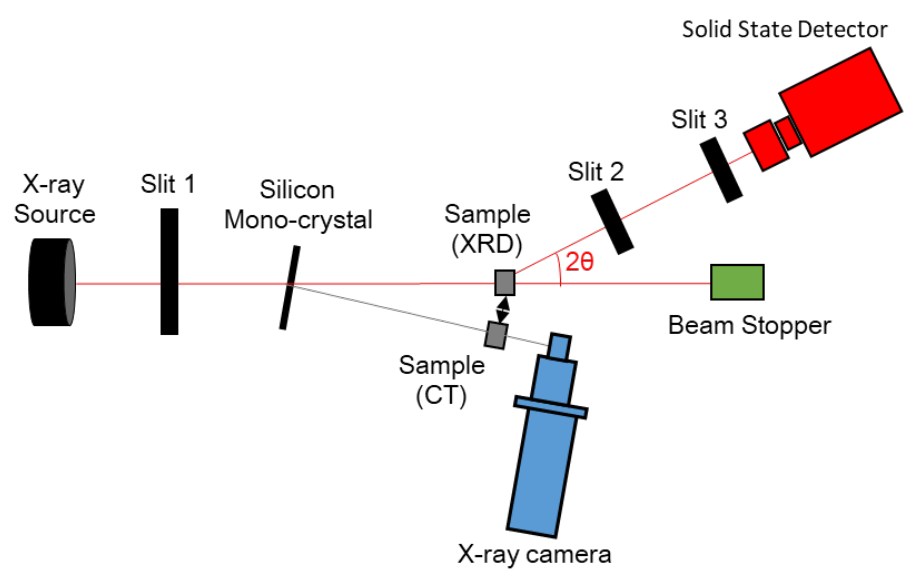
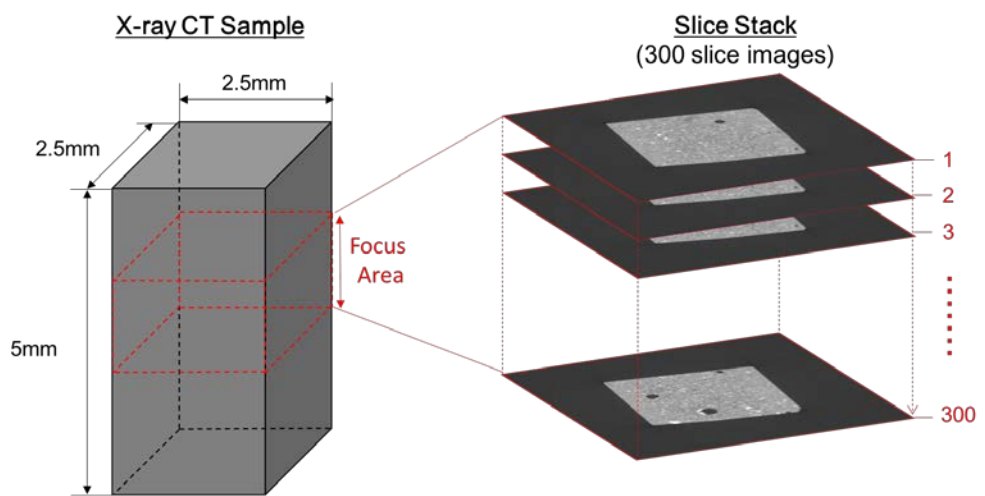


Figure 1 Overview of experimental program



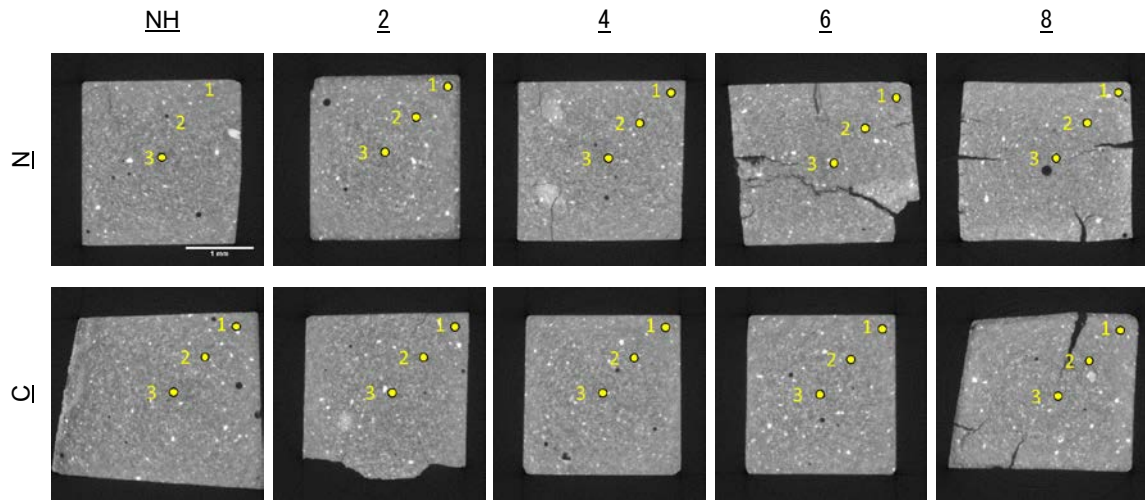
8
9
10
11
12

Figure 2 Schematic diagram of the system for non-destructive integrated CT-XRD method

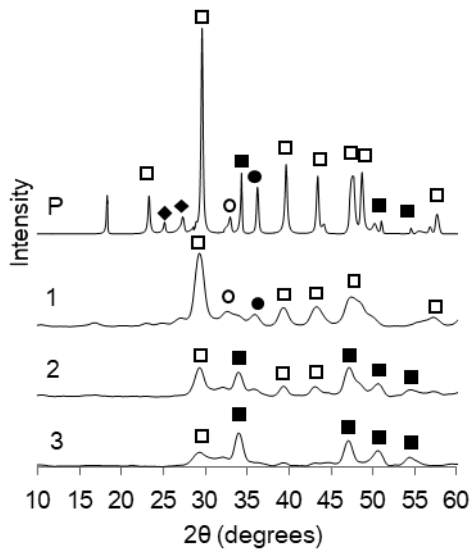


13
14

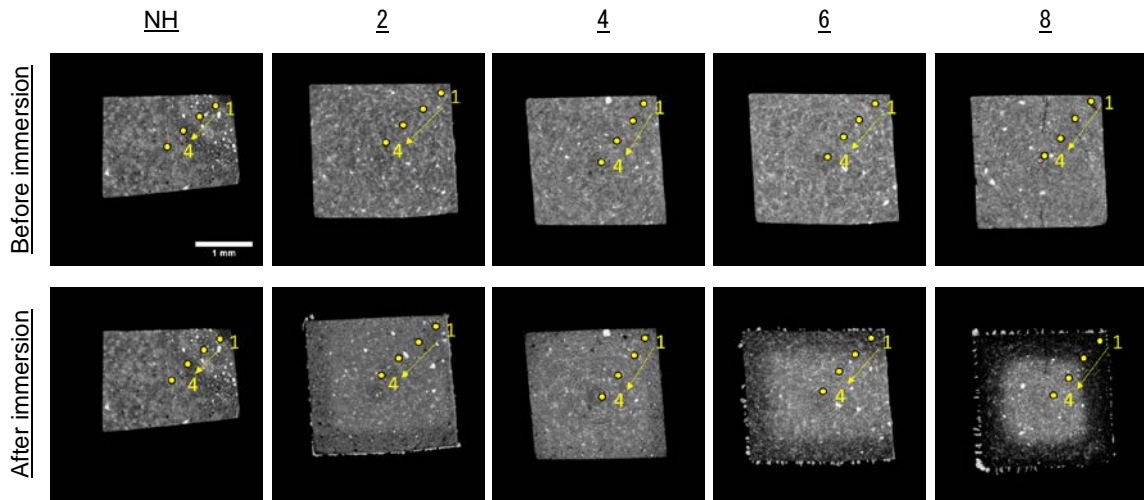
Figure 3 Image analysis area in CT measurement



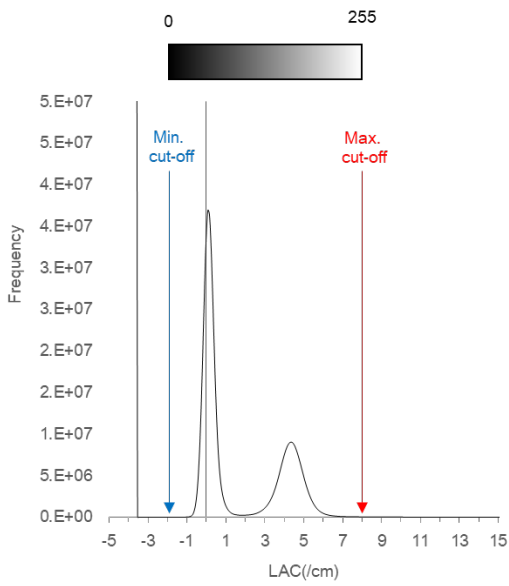
1
 2 Figure 4 Cross sectional images at center heights in Experiment I. The markers indicate
 3 the position of XRD measurement
 4
 5



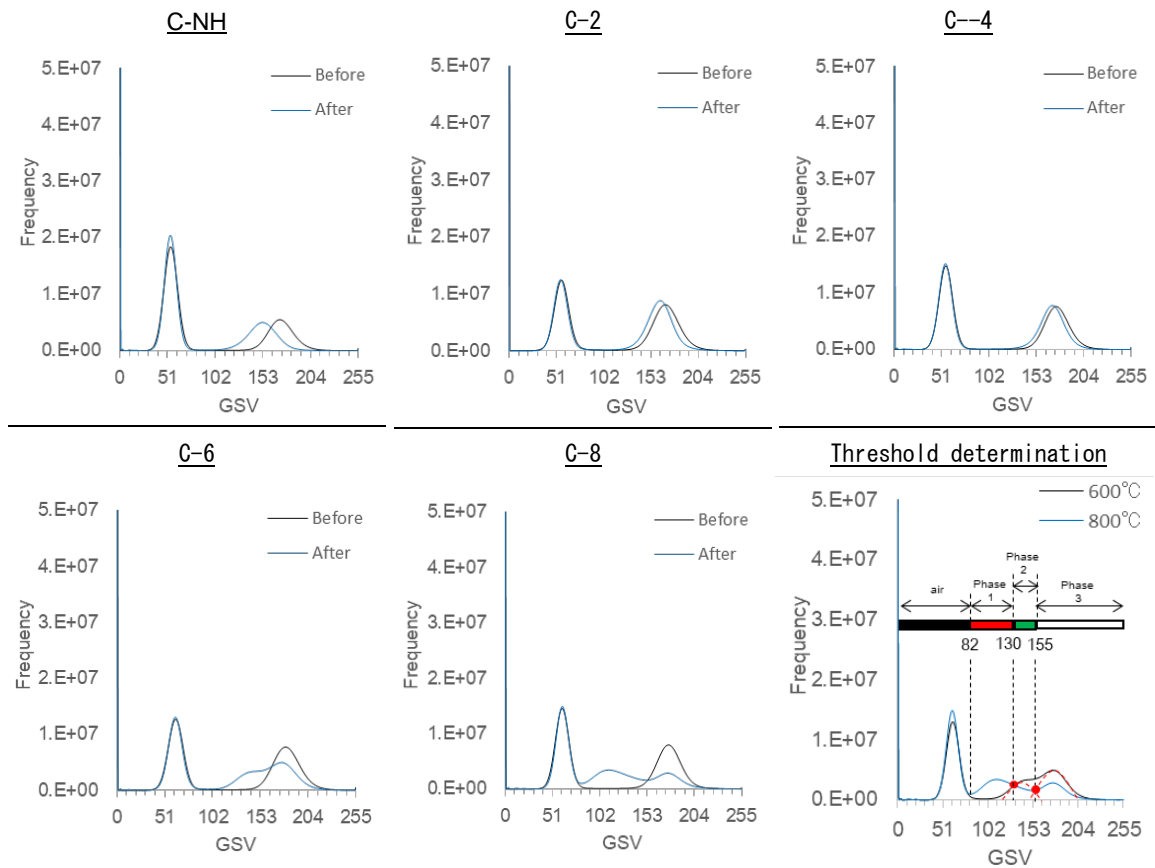
6
 7
 8 Figure 5 XRD profiles of C-NH by P-XRD (P) and the CT-XRD (1, 2, and 3)
 9 (alite:▲, belite:○, portlandite:■, calcite:□, vaterite:◆, lime:●)
 10
 11
 12
 13
 14
 15
 16
 17
 18
 19



1
 2 Figure 6 Cross sectional images at center heights in Experiment II. The markers indicate
 3 the position of XRD points.
 4
 5



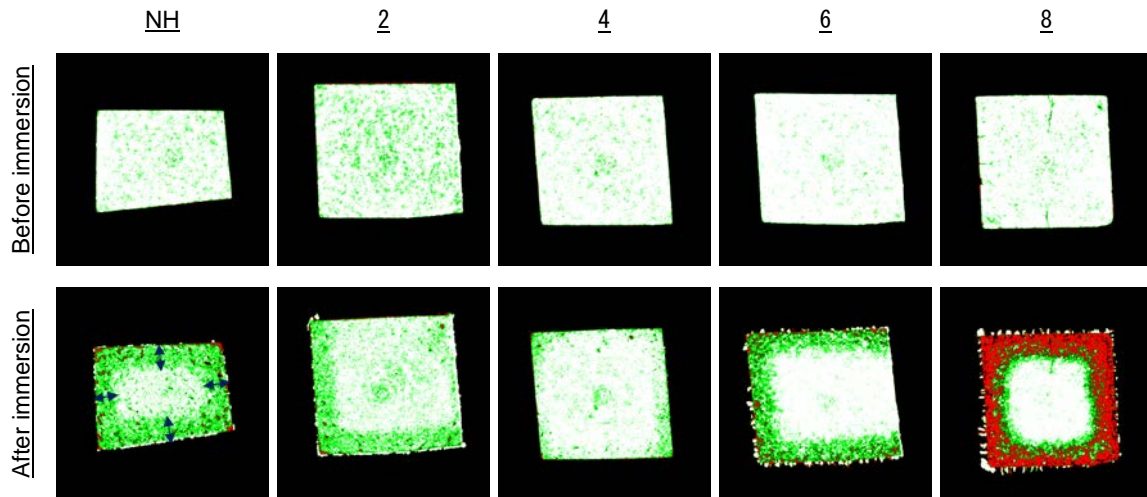
6
 7
 8 Figure 7 Example of CT histogram of the CT images and rescaling to 8bit gray scale
 9 images
 10
 11
 12
 13
 14
 15
 16
 17
 18
 19



1
2 Figure 8 Histograms of each sample before and after immersion and threshold
3 determination for phase segmentation
4

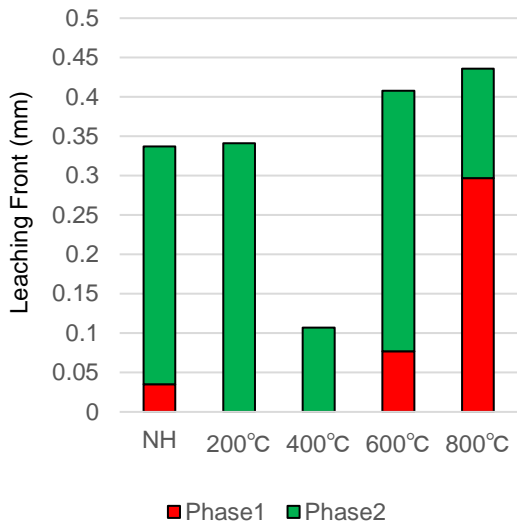
	Cathode Side	Anode Side		
Area Division	Phase 1	Phase 2	Phase 3	Phase 4
Phase Composition	SiO_2	C-S-H	C-S-H	C-S-H, CH
Ca/Si ratio in C-S-H		low	normal	normal

5
6
7 Figure 9 Schematic diagram of alteration mechanism with calcium leaching (revised Ref.
8 [33])
9
10
11
12
13
14
15



1
2
3
4
5
6
7

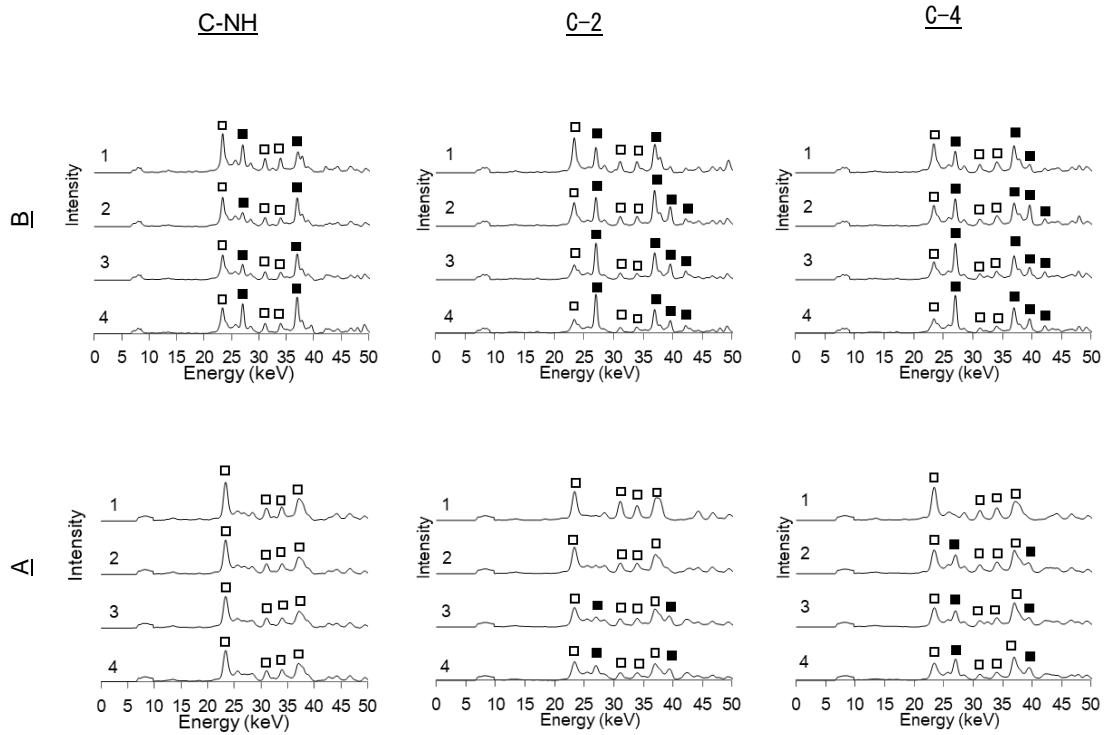
Figure 10 Region of Interest extracted from original data set and visualization of leaching area from phase segmentation (colored as phase 1 in red, phase 2 in green, and phase 3 & 4 in white, both ends arrows in After immersion of NH show an example of measurement points of leaching front



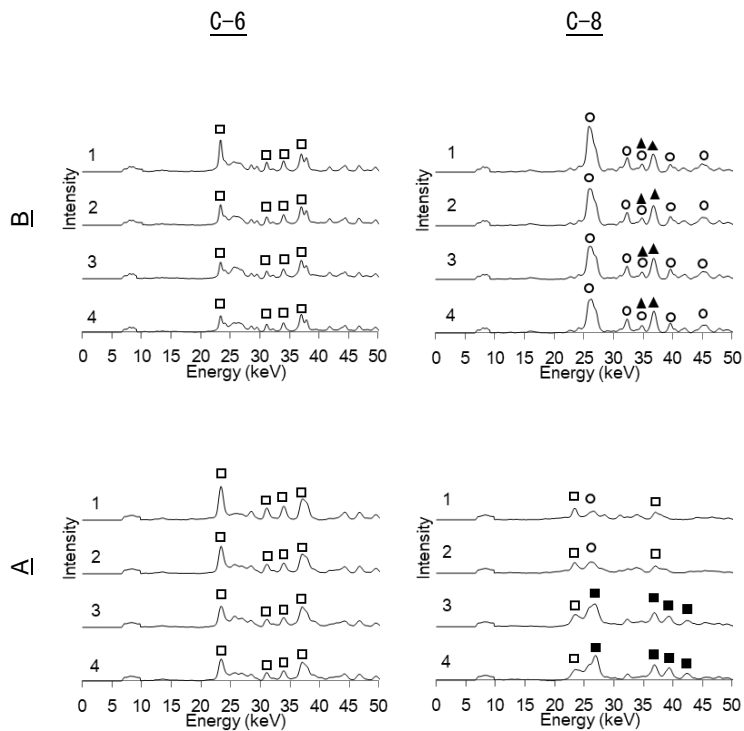
8
9
10
11
12
13
14
15
16
17
18
19
20

Figure 11 Leaching front for each sample measured from segmented images

1



2



3

4 Figure 12 XRD profiles of all samples before and after immersion by the CT-XRD (1, 2,
5 3, and 4) (alite: ▲, belite: ○, portlandite: ■, calcite: □, vaterite: ◆, lime: ●)